APPLIED PHYSICS

2D metal-organic frameworks for ultraflexible electrochemical transistors with high transconductance and fast response speeds

Jiajun Song[1], Hong Liu[1], Zeyu Zhao[1], Xuyun Guo[1], Chun-ki Liu[1], Sophie Griggs[2], Adam Marks[2], Ye Zhu[1], Helen Ka-wai Law[3], Iain McCulloch[2], Feng Yan[1,4]*

Electrochemical transistors (ECTs) have shown broad applications in bioelectronics and neuromorphic devices due to their high transconductance, low working voltage, and versatile device design. To further improve the device performance, semiconductor materials with both high carrier mobilities and large capacitances in electrolytes are needed. Here, we demonstrate ECTs based on highly oriented two-dimensional conjugated metal-organic frameworks (2D c-MOFs). The ion-conductive vertical nanopores formed within the 2D c-MOFs films lead to the most convenient ion transfer in the bulk and high volumetric capacitance, endowing the devices with fast speeds and ultrahigh transconductance. Ultraflexible device arrays are successfully used for wearable on-skin recording of electrocardiogram (ECG) signals along different directions, which can provide various waveforms comparable with those of multilead ECG measurement systems for monitoring heart conditions. These results indicate that 2D c-MOFs are excellent semiconductor materials for high-performance ECTs with promising applications in flexible and wearable electronics.

INTRODUCTION

Electrolyte-gated transistors (EGTs) have been regarded as a fundamental building block in numerous applications including wearable/implantable electronics (*1*–*5*), neuromorphic devices (*6*–*9*), and low-voltage circuits (*10*–*12*). As a subclass of thin-film transistors, EGT has a similar device structure to a conventional field-effect transistor (FET), while the solid-state gate dielectric layer in the FET is substituted with an electrolyte (liquid, gel, and solid) that connects the channel and the gate electrode of the EGT. Hence, EGTs operating in electrolytes, particularly aqueous solutions, are inherently advantageous for bioelectronic applications (*13*). Transconductance ($g_m = \partial I_{DS}/\partial V_{GS}$) is a key parameter for a transistor to convert a voltage signal applied on its gate (V_{GS}) into a channel current response (I_{DS}). EGTs normally show high transconductance and thus can be used as amplifiers in various sensing applications, such as chemical sensors and biosensors (*14*–*16*). The transconductance of a transistor is proportional to the product of μC, where μ is the carrier mobility in the channel and C is the gate capacitance (*13*, *17*). EGTs have been realized on the basis of various materials such as graphene (*3*, *4*, *18*), transition metal dichalcogenides (*19*), amorphous metal oxides (*20*), and organic semiconductors (*8*, *21*, *22*). To date, electrolyte-gated organic transistors known as organic electrochemical transistors (OECTs) show the highest transconductance due to their high gate capacitances (*21*, *23*). To further improve the device performance of EGTs, materials with both high carrier mobilities and large capacitances in electrolytes are needed.

Two-dimensional conjugated metal-organic frameworks (2D c-MOFs), an emerging class of nanoporous crystalline materials, have attracted much research interests for their great potential in numerous applications like catalysis, gas sensors, and energy storage (*24*–*26*). In 2D c-MOFs, the extended 2D π-conjugated lattice (in-plane) formed by linking the ortho-substituted conjugated organic ligands with metal nodes is orderly stacked along the out-of-plane direction via π-π stacking interactions (*25*). This unique structure awards 2D c-MOFs appealing charge transport properties without compromising the advantages of conventional MOFs including ordered porous structures and large surface areas, which have promoted their implementations in electronic devices including batteries (*27*, *28*), FETs (*29*, *30*), and supercapacitors (*31*). Notably, the combination of high carrier mobilities and huge bulk capacitances of 2D c-MOFs in electrolytes promise their applications in EGTs, which however have been rarely reported until now.

Here, we report ambipolar electrochemical transistors (ECTs) based on a 2D c-MOF $Cu_3(HHTP)_2$ [2,3,6,7,10,11-hexahydroxytriphenylene (HHTP)] and demonstrate the applications in flexible electronics for multidirectional electrocardiogram (ECG) mapping. Highly oriented 2D c-MOF films along [001] were prepared by a reproducible layer-by-layer growth method and used as the channel material in MOF-based ECTs (MOFECTs). Large-area MOFECT arrays were fabricated by a convenient microfabrication process, achieving a high device yield with a rather uniform carrier mobility distribution. The MOFECTs exhibit balanced hole and electron transport properties, in which the bulk conductivity of $Cu_3(HHTP)_2$ can be substantially modulated through cations or anions doping from the electrolyte. Notably, we find that the high-porosity crystal structure of the [001]-oriented 2D c-MOF film facilitates ion diffusion in the bulk across vertical nanopores, leading to a high volumetric capacitance C^* of 67.8 F cm^{-3}, a fast response (10 μs), and an ultrahigh μC value of n-channel ECTs. Large-area MOFECT arrays are successfully fabricated on ultrathin

[1]Department of Applied Physics, The Hong Kong Polytechnic University, Hung Hom, Kowloon, 999077 Hong Kong, People's Republic of China. [2]Department of Chemistry, University of Oxford, Oxford OX1 3TA, UK. [3]Department of Health Technology and Informatics Faculty of Health and Social Sciences, The Hong Kong Polytechnic University, Hung Hom, Kowloon 999077, Hong Kong, People's Republic of China. [4]Research Institute of Intelligent Wearable Systems, The Hong Kong Polytechnic University, Hung Hom, Kowloon 999077, Hong Kong, People's Republic of China.
*Corresponding author. Email: apafyan@polyu.edu.hk

flexible substrates with uniform and stable performance. The flexible device arrays are conformally attached on a human body and successfully used for spatial mapping of ECG signals along different directions for the first time, which is much more convenient than conventional multilead ECG measurements.

RESULTS

Microfabrication of MOFECTs

2D c-MOF $Cu_3(HHTP)_2$ films were prepared by a layer-by-layer growth method. To study the crystal structure and orientation of the films, in-plane and out-of-plane x-ray diffraction patterns were measured using grazing incidence x-ray diffraction (GIXRD). In the in-plane XRD pattern (fig. S1A), three 2θ diffraction peaks at 4.6°, 9.4°, and 12.6° are observed, corresponding to the (100), (200), and (210) planes, respectively. In comparison, only a featured peak at 2θ = 28.0° can be observed in the out-of-plane XRD profile, corresponding to the (002) plane (*32*). The GIXRD patterns indicate the successful formation of $Cu_3(HHTP)_2$ with an in-plane hexagonal lattice, which adopts preferential orientated growth along [001] direction on the substrate in a slipped-parallel AB stacking mode (Fig. 1A) (*32*). The average crystallite size of the MOF is estimated to be ~28 nm by using Williamson-Hall (W-H) method (fig. S1B and Materials and Methods) (*33*), revealing the polycrystalline character of the $Cu_3(HHTP)_2$.

$Cu_3(HHTP)_2$ thin films were peeled off from substrates and characterized under a high-resolution transmission electron microscopy (HRTEM). The HRTEM image and the corresponding Fast Fourier transform (FFT) pattern (Fig. 1B) clearly indicate the hexagonal nanoporous structure of $Cu_3(HHTP)_2$ with a ~1.9-nm lattice spacing, which provides vertical channels for ion diffusion into the bulk of the MOF films in an electrolyte, as depicted in Fig. 1A. In addition, the electron energy loss spectroscopy mapping (fig. S2) indicates the uniform distribution of C, Cu, and O atoms over the entire film, verifying the chemical composition of $Cu_3(HHTP)_2$.

The morphology of $Cu_3(HHTP)_2$ films was characterized under scanning electronic microscopy and atomic force microscopy (fig. S3), demonstrating continuous and complete coverages on the substrates. The film thickness is proportional to the number of layer-by-layer growth cycles, and the increased thickness for each growth cycle is about 10 nm (fig. S4). The average surface roughness of the film increases linearly with the growth cycles (fig. S5). Moreover, the $Cu_3(HHTP)_2$ films were found to be hydrophilic from contact angle measurements (contact angle: 66.92°; fig. S6), which enables ion diffusion into the films in aqueous solutions. The light absorption spectrum of a $Cu_3(HHTP)_2$ film clearly shows an optical bandgap of about 0.22 eV (fig. S7), implying that MOFECTs based on $Cu_3(HHTP)_2$ would show ambipolar behavior because of the small bandgap energy.

Figure 1C presents the device architecture of a MOFECT, in which a layer of 2D c-MOF $Cu_3(HHTP)_2$ is patterned in the channel region between source and drain electrodes (Fig. 1D) by a reproducible photolithography process (Fig. 1E and Materials and Methods). A metal gate electrode is patterned on the same substrate, and the device can operate with an electrolyte covering both the gate and the channel region.

The performance of MOFECTs based on $Cu_3(HHTP)_2$ was characterized by coating a 0.05 M $CaCl_2$ aqueous solution on the devices as an electrolyte. Figure 2 (A and B) present the output

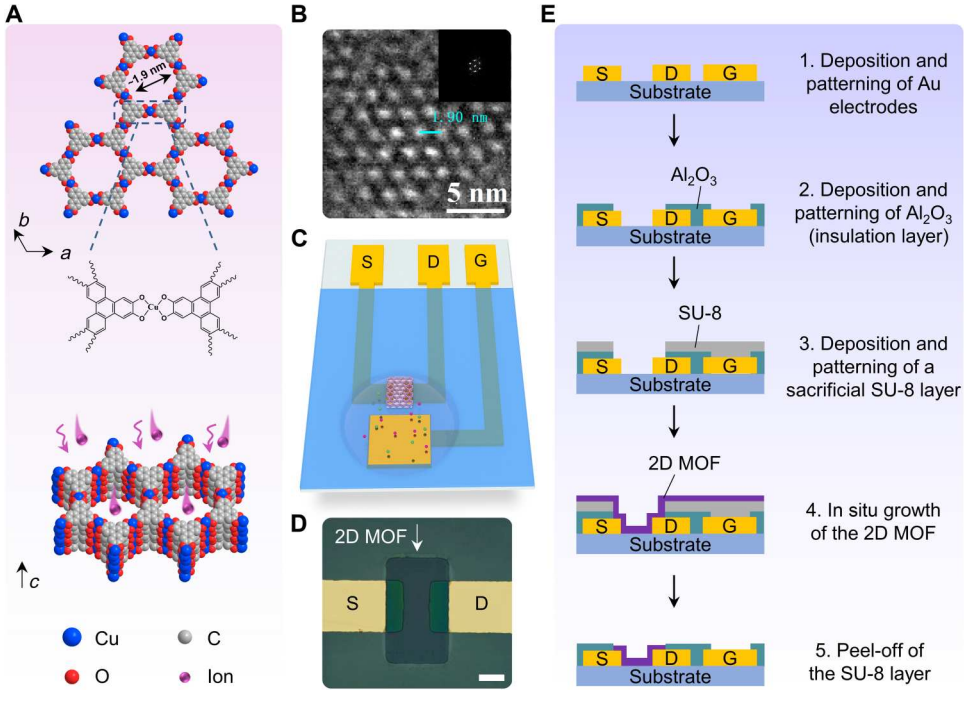

Fig. 1. Microfabrication of MOFECTs. (**A**) Structure of $Cu_3(HHTP)_2$ and the diagram of the ion doping process within the vertical nanopores. Hydrogen atoms are hidden for clarity. (**B**) HRTEM image of a $Cu_3(HHTP)_2$ film. Insert: FFT of the area. (**C**) Device architecture of a MOFECT based on $Cu_3(HHTP)_2$. (**D**) Optical micrograph of the channel of a device. Scale bar, 30 μm. (**E**) Microfabrication process flow of MOFECTs.

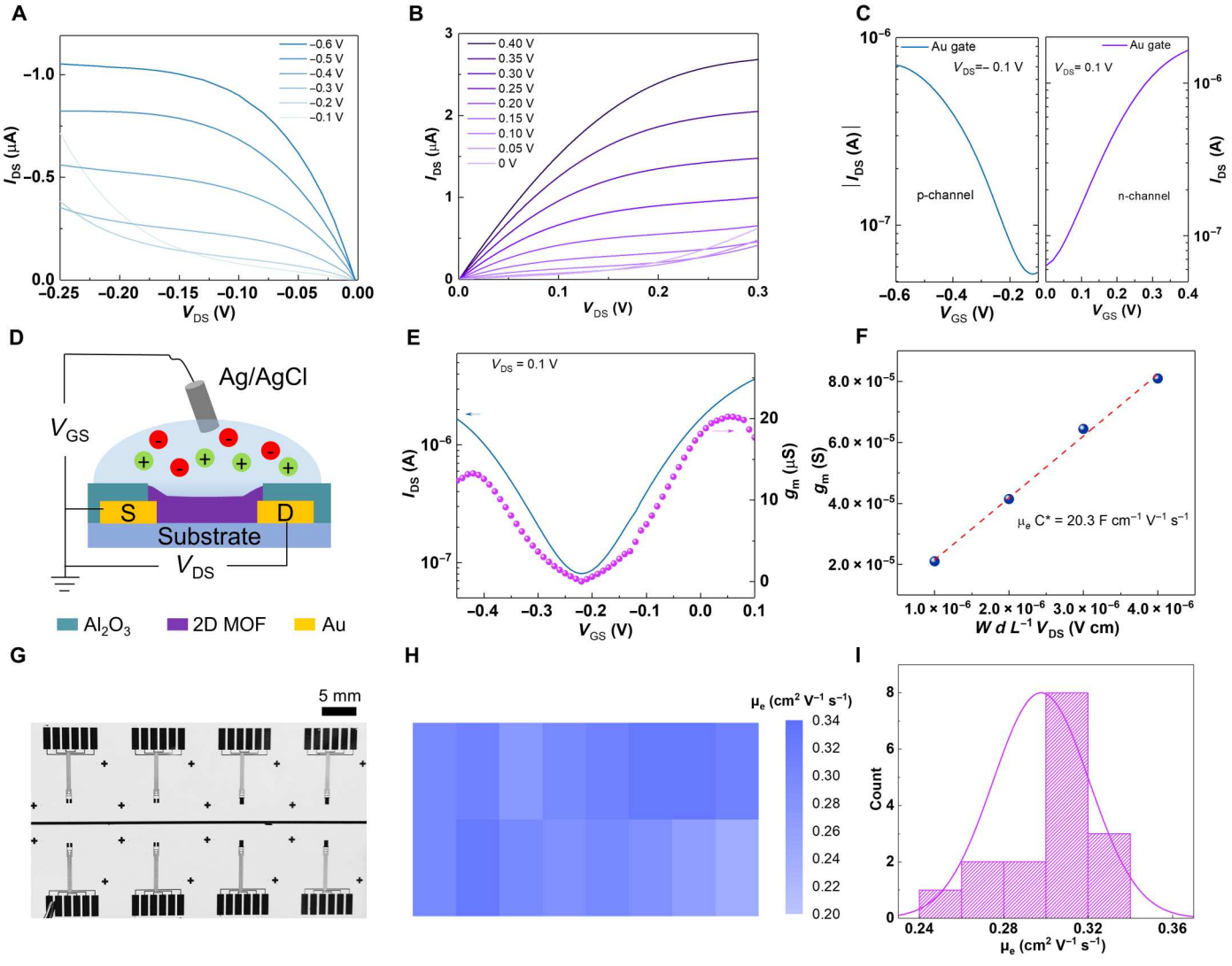

Fig. 2. Figures of merit of MOFECTs. (**A**) Output characteristics of a MOFECT in p-type operation and (**B**) in n-type operation. (**C**) Transfer curves of the MOFECT in ambipolar operation. (**D**) Diagram of the MOFECT with a Ag/AgCl gate. (**E**) Transfer curve (V_{DS} = 0.1 V) of an ambipolar MOFECT with a Ag/AgCl gate. (**F**) Estimation of the $\mu_e C^*$ product according to the dependence of peak transconductance on the geometric and operational parameters. The transconductance is tuned by changing the film thickness from 50 to 200 nm. (**G**) Photograph of MOFECT arrays (16 individual devices) on a large-area substrate (30 mm by 50 mm). (**H**) Mapping of the electron mobilities of $Cu_3(HHTP)_2$ on the substrate. (**I**) Histogram and distribution of the electron mobilities extracted from 16 MOFECTs.

characteristics of a MOFECT (channel thickness d = 50 nm, channel width W = 60 μm, channel length L = 30 μm) in p- and n-channel operation, respectively, which clearly display the typical linear, nonlinear, and saturation regions of the transistor. The corresponding transfer characteristics (I_{DS} versus V_{GS}) of the MOFECT are depicted in Fig. 2C. When a higher positive gate voltage is applied to the device, more cations in the electrolyte permeate into the vertical porous channels, causing an n-type doping of $Cu_3(HHTP)_2$ and thereby an increased bulk conductivity. In contrast, the application of a negative gate bias drives anions into the channel, leading to a p-type doping of $Cu_3(HHTP)_2$. Hence, the MOFECTs exhibit an ambipolar behavior, in which the channel current (I_{DS}) flowing through the $Cu_3(HHTP)_2$ channel can be modulated via both cations and anions doping from the electrolyte under different gate voltages (V_{GS}). Notably, the leakage current I_{GS} is negligible, as shown in fig. S8, indicating the effective encapsulation of the metal interconnection by Al_2O_3.

Figures of merit of MOFECTs

To accurately extract the figures of merit of the MOFECTs, a nonpolarizable electrode, Ag/AgCl (sat. KCl), instead of an in-plane Au electrode was used as the gate (Fig. 2D). A notable shift of the transfer curve (Fig. 2E) toward negative voltage can be observed in the MOFECT due to the electrochemical potential of the Ag/AgCl (sat. KCl) electrode. The device exhibits peak transconductances g_m of 20.2 and 13.3 μS for n- and p-type operation, respectively, indicating balanced electron and hole transport in the channel.

The ordered vertical nanopores in $Cu_3(HHTP)_2$ films can provide unimpeded pathways for ion diffusion and thereby lead to volumetric doping of the films. Consequently, the performance

of MOFECTs can be notably tailored by changing the channel thickness (*34*). Hence, we characterized the thickness effect of the $Cu_3(HHTP)_2$ channels on the device performance. According to the n-channel transfer curves of MOFECTs with different channel thicknesses (fig. S9), we obtained the peak transconductance g_m of the MOFECTs, which increases linearly with the channel thickness (Fig. 2F). Notably, negligible hysteresis was observed between the forward and reverse scans of the transfer curves, implying that the bulk doping of $Cu_3(HHTP)_2$ is fast and reversible. The devices exhibit a high geometry-normalized transconductance $g_{m,\,nom}$ = 2.0 S cm^{-1} ($g_{m,nom} = g_m \frac{L}{Wd}$, where W, L, and d are the width, length, and thickness of the channel, respectively) at a very low working voltage V_{DS} = 0.1 V, which is comparable to the best performance of conventional n-type OECTs (*35*, *36*). For the n-channel MOFECT operating in the linear region ($|V_{DS}| < |V_{GS} - V_{TH}|$), transconductance g_m is given by (*37*, *38*)

$$g_m = \left(\frac{Wd}{L}\right) \cdot \mu_e \cdot C^* \cdot V_{DS} \quad (1)$$

where C^* is the capacitance per unit volume of the channel, V_{DS} is the source-drain voltage. Linear fitting of the curve in Fig. 2F yields a slope ($\mu_e C^*$ product) of 20.3 F cm^{-1} V^{-1} s^{-1}, which is comparable to that of the best n-channel OECTs (*35*, *36*). Similarly, the $\mu_h C^*$ product of the p-channel MOFECT is estimated to be 13.4 F cm^{-1} V^{-1} s^{-1}. Notably, the product ($\mu C^* d$, d = 200 nm) of carrier mobility and capacitance per unit area of MOFECTs is much higher than those of conventional FETs based on various semiconductors (table S1) (*39*–*42*), enabling a superior transconductance of the device under a low working voltage, which is advantageous for bioelectronic applications.

The volumetric capacitance C^* of $Cu_3(HHTP)_2$ can be extracted by measuring the electrochemical impedance spectroscopy (EIS) of the MOF films with different thicknesses. As shown in fig. S10, the capacitance value under a bias of −0.05 V applied on the working electrode (equivalent to V_{GS} = 0.05 V) increases linearly with the thickness of $Cu_3(HHTP)_2$, yielding a volumetric capacitance C^* of 67.8 F cm^{-3} for n-type doping. Thus, the electron mobility (μ_e) of $Cu_3(HHTP)_2$ is estimated to be 0.30 cm^2 V^{-1} s^{-1}, which is similar to the best n-type OECT reported before (*36*). Similarly, the volumetric capacitance C^* for p-type doping under a 0.50 V bias applied on the working electrode, which is equivalent to the gate voltage V_{GS} = −0.50 V applied on the MOFECTs, was measured to be 84.9 F cm^{-3} (fig. S11). Hence, the hole mobility of $Cu_3(HHTP)_2$ is estimated to be 0.16 cm^2 V^{-1} s^{-1}. The high charge carrier mobility of $Cu_3(HHTP)_2$ can be attributed to its extended in-plane π-conjugation, which facilitates the delocalization of charge carriers.

To gain more insights into the volumetric doping of the MOFECT, we carried out ex situ x-ray photoelectron spectroscopy (XPS) characterizations of MOF films before and after ion doping at the biases of −0.5 and 0.05 V via a Ag/AgCl electrode. The XPS survey (fig. S12A) reveals the presence of Cu, O, and C elements in the film, confirming the chemical composition of $Cu_3(HHTP)_2$. The high-resolution XPS spectra of Cu 2*p* (fig. S12B) indicate the coexistence of Cu^{2+} (~934.6 eV) and Cu^+ (~932.8 eV) in the $Cu_3(HHTP)_2$, which is consistent with results in literature (*32*). The relative ratio of Cu^+ to Cu^{2+} can be obtained from the deconvolution of the Cu $2p_{3/2}$ spectra, which shows negligible change after n-type and p-type doping. The O 1*s* XPS spectrum (fig. S12C) incorporates two peaks at ~532.5 and ~531.2 eV, suggesting that the HHTP ligand can adopt benzoid and quinoid structures (*28*). The deconvoluted results suggest invariable valence of O after ion doping. These results imply that no pronounced redox process occurs in the 2D MOF after ion doping within the operational voltage region with a Ag/AgCl gate. Thus, the ion doping in the device is considered to be an electrostatic behavior.

Benefiting from the convenient liquid-phase deposition of $Cu_3(HHTP)_2$, large-area fabrication of MOF transistor arrays has been realized. As shown in Fig. 2G, MOFECT arrays containing 16 individual devices were successfully fabricated on a large-area substrate (30 mm × 50 mm). The transfer curves of the devices are presented in fig. S13. The electron mobilities extracted from the MOFECTs located at different positions are mapped in Fig. 2H, indicating uniform device performance on the entire substrate. The devices show a narrow mobility distribution between 0.24 and 0.32 cm^2 V^{-1} s^{-1} with an average value of 0.30 ±0.02 cm^2 V^{-1} s^{-1} (Fig. 2I).

Transient response and operational stability of transistors are critical to their practical applications. To evaluate the switching speed of MOFECTs in n-type operation, gate voltage pulses (ΔV_{GS} = 0.3 V) were applied, and the temporal response of channel current was monitored. As shown in Fig. 3A, the channel current exhibits fast and reproducible switching under pulsed V_{GS}. By fitting the rising edge with an exponential function, the response time is extracted to be 0.88 ms. To explore the limit of switching speed of MOFECTs, the devices were further miniaturized with the channel length and width of 2 and 50 μm, respectively. As shown in Fig. 3B, the MOFECT with a shorter channel exhibits a fast response time of 10 μs, which is much faster than n-type OECTs with a similar channel thickness (fig. S14) (*35*, *36*, *43*–*45*). The fast response speed can be attributed to the vertical ion-conductive nanopores in the 2D c-MOF crystal, which lead to more convenient ion transport across the 2D c-MOF film than in a typical organic semiconductor film (fig. S15).

The transient response time of a MOFECT is limited by two factors, including carrier transport in electronic circuit (within the channel) and ion transport in ionic circuit (electrolyte-to-channel) (*37*). The transient time for carriers to travel from source to drain is given by $\tau_e \approx \frac{L^2}{\mu V_{DS}}$, where L is the channel length, μ is the average carrier mobility, and V_{DS} is the drain voltage. For n-channel, the average carrier mobility under different gate voltage is calculated to be 0.17 cm^2 V^{-1} s^{-1}. Hence, the transient times τ_e are estimated to be 0.53 ms and 2.4 μs for the channel length of 30 and 2 μm, respectively. For the device with the channel length of 30 μm, the response time (0.88 ms) to a gate bias is close to the transient time of electrons across the channel, indicating that the response speed is mainly limited by electron transport. However, for the device with the channel length of 2 μm, the response time (10 μs) is much longer than the electron transit time. Therefore, the transient response of the device with a short channel is determined by ion transport.

Ion injection in a 2D c-MOF film with vertical nanopores can be described by a transmission line model (*26*, *46*). The charge $Q(t)$ injected into the 2D c-MOF channel under a gate voltage pulse is

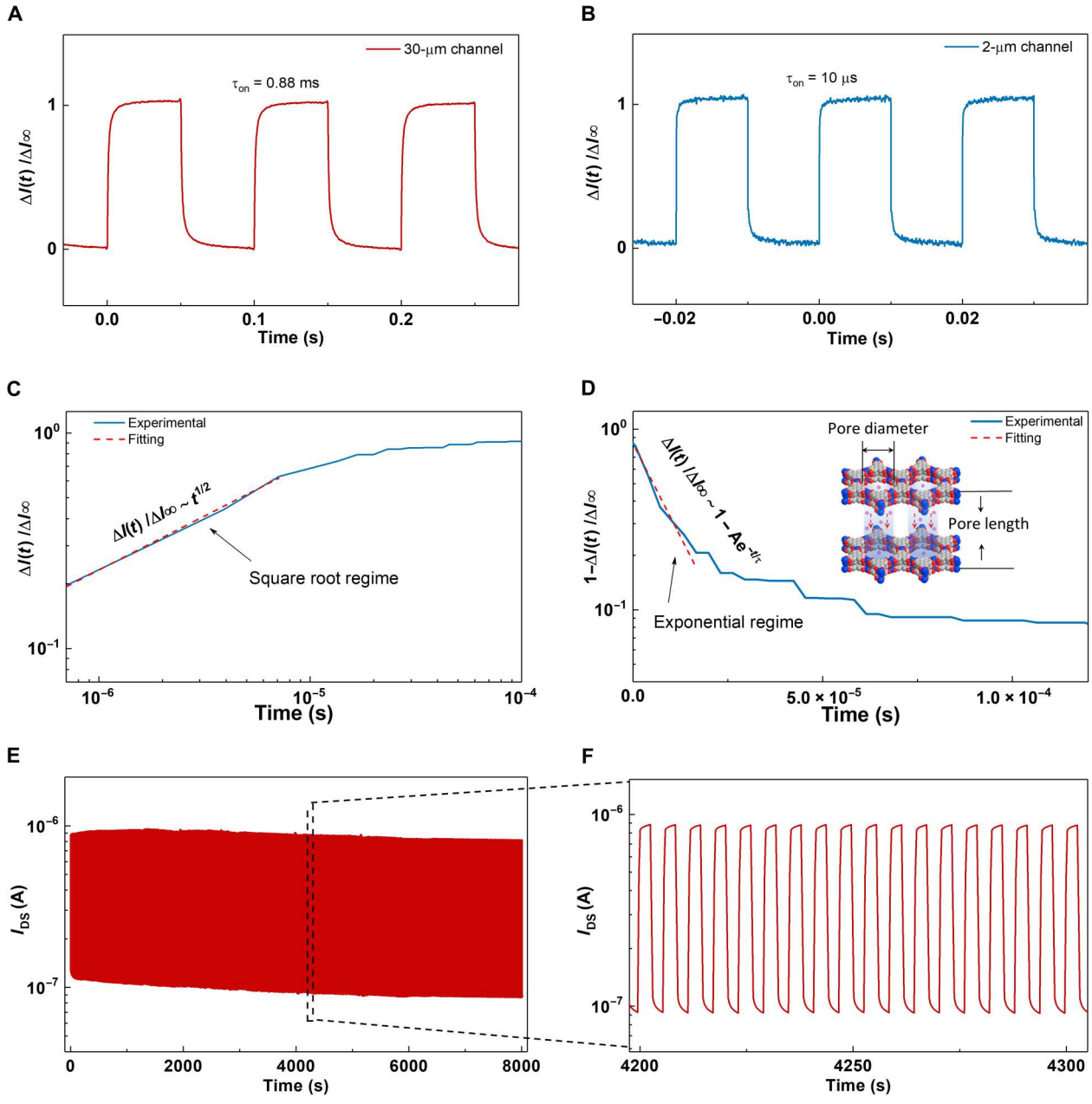

Fig. 3. Transient response and stability of MOFECTs. (**A**) Transient response of the channel current (ΔV_{GS} = 0.3 V, V_{DS} = 0.1 V) of a MOFECT (W = 60 μm, L = 30 μm, channel thickness: 50 nm). (**B**) Transient response of the channel current (ΔV_{GS} = 0.3 V, V_{DS} = 0.1 V) of a MOFECT with a short channel (W = 50 μm, L = 2 μm, channel thickness: 50 nm). (**C**) Fitting of the channel current response (device with a 2-μm channel) with a square root law at the initial stage. (**D**) Fitting of the channel current response (device with a 2-μm channel) with an exponential function in a longer period. Insert is a diagram of the ion diffusion within the vertical nanopores. (**E**) Operational stability test of a MOFECT under sequential pulsed V_{GS} for 8000 s (ΔV_{GS} = 0.3 V, pulse period = 6 s, V_{DS} = 0.1 V), including (**F**) an enlargement around t = 4250 s.

given by

$$Q(t) = Q_\infty \left\{ 1 - \frac{2}{\pi^2} \sum_{n=0}^{\infty} \frac{\exp\left[-\pi^2 \left(n+\frac{1}{2}\right)^2 \left(\frac{2l}{H}\right)^2 \frac{t}{\tau}\right]}{\left(n+\frac{1}{2}\right)^2} \right\} \quad (2)$$

where Q_∞ is the fully charged amount under the gate bias, l is the pore volume divided by its surface area, H is the length of the vertical pore, and τ is the intrinsic relaxation time. Here, l is estimated to be 0.46 nm (table S2) for $Cu_3(HHTP)_2$ crystal, and H is equal to the film thickness. τ is given by $\tau = \frac{C_{area} l}{\sigma}$, where C_{area} is the areal capacitance of the nanopore ($C_{area} \approx 5.9$ μF cm^{-2} for n-type doping; table S2) and σ is the conductivity of the electrolyte in the nanopore. According to the analytical model, $Q(t)$ is proportional to $\sqrt{t}$ in a short period of time and can be described with an exponential function $Q(t) \approx Q_\infty \{1 - \frac{8}{\pi^2} \exp[-\frac{t}{\tau(\frac{H}{l})^2}]\}$ in a longer period.

Injected ions induce the same amount of carriers with an opposite sign in the transistor channel. Hence, the channel current

response $\Delta I_{DS}(t)$ is proportional to $Q(t)$. As shown in Fig. 3C, the channel current can be fitted with an equation $\Delta I(t)/\Delta I_\infty \sim \sqrt{t}$ at the initial stage, where ΔI_∞ is the stabilized current increase. Then, the current can be fitted with an exponential function $\Delta I(t)/\Delta I_\infty \approx 1 - A\exp(-t/\tau_0)$ in a longer period, as shown in Fig. 3D, where τ_0 is the time constant, which is given by $\tau_0 = \tau\left(\frac{H}{l}\right)^2$. Hence, the ion conductivity σ in the pore can be estimated to be 0.032 S m^{-1}. It is reasonable to find that the ion conductivity in the nanopores is lower than in aqueous solution (0.60 S m^{-1} for 0.05 M Ca^{2+}) (*26*, *47*). All the results confirm that the channel current response is limited by ion diffusion across the vertical nanopores in the $Cu_3(HHTP)_2$ film. Notably, the response time is proportional to H^2, indicating that fast-response devices can be achieved by using a thin active layer. Hence, we should have a trade-off between the response speed and transconductance in device design for specific applications. The transient response of the p-channel MOFECT with a 2-μm channel was also characterized (fig. S16), which shows a fast response of 49 μs. As the response time is much longer than the hole transit time (~4.7 μs) within the channel, the transient response of the p-type device with a short channel is also dominated by ion transport. Thus, the difference between the transient response of the n-type and p-type devices could be attributed to the variations in ionic conductivities and areal capacitance in the nanopores.

Long-time operational stability testing was carried out by applying continuous gate pulses. As presented in Fig. 3 (E and F), the n-channel device (ΔV_{GS} = 0.3 V, pulse period = 6 s) shows good stability under stress testing as the channel current degradation is less than 9% after more than 10^3 successive pulses in 8000 s. The excellent stability of the n-type MOFECT in the aqueous electrolyte can be attributed to the deep lowest unoccupied molecular orbital level (−4.74 eV) of $Cu_3(HHTP)_2$ (*32*), which can resist the oxidation by water and oxygen (*48*). The p-channel device also shows good stability with a channel current degradation less than 11% (fig. S17) after a similar stress testing (ΔV_{GS} = 0.5 V, pulse period = 6 s).

In addition, benefiting from the high crystallinity of $Cu_3(HHTP)_2$, the film swelled negligibly in the aqueous electrolyte, as no increase in the film thickness (fig. S18) could be observed when the film was exposed to electrolyte under a bias voltage. In conventional OECTs, the swelling of organic channels should be carefully treated, as an optimized hydration of polymers is commonly suggested to enable efficient ion doping of the bulk organic channel, while excessive swelling could harm the charge carrier mobility and reversibility of electrochemical doping and lead to poor stability of the material (*49*–*51*). No swelling of $Cu_3(HHTP)_2$ films in electrolytes implies better stability and reversibility of the devices. Hence, $Cu_3(HHTP)_2$ shows inherent advantages in the applications as the channel materials of ECTs, which can achieve high carrier mobility, fast switching, large volumetric capacitance, and stability.

Implementations of MOFECTs in flexible inverters

A complementary inverter is the building block for integrated circuits, which is composed of a p-type and an n-type transistor or two ambipolar transistors (*52*). With the upsurge of battery-powered

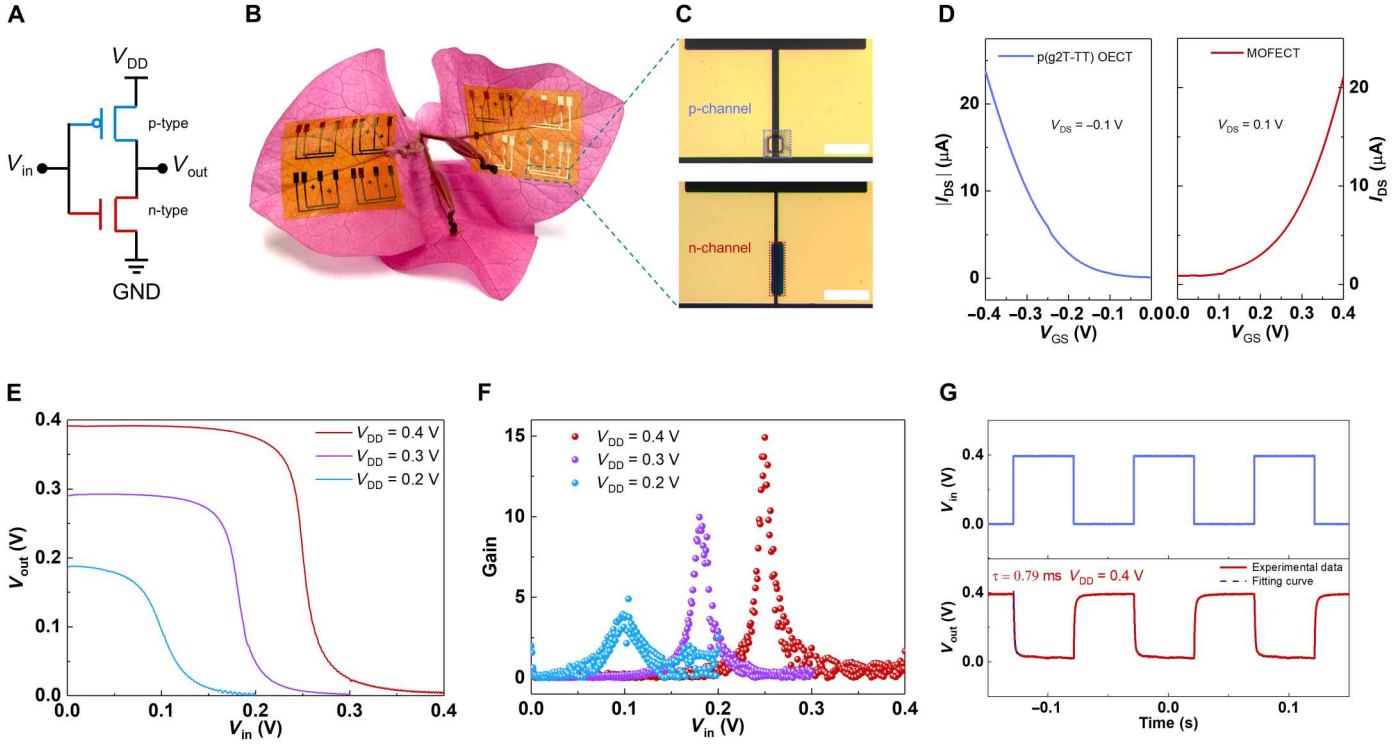

Fig. 4. Implementations of MOFECTs in flexible circuits. (**A**) Circuit schematic of a complementary inverter. GND: Ground. (**B**) Photograph of the ultrathin flexible inverters laid on the soft bracts of *B. glabra*. (**C**) Microscope photos of the patterned channels of an inverter. Scale bar, 40 μm. (**D**) Transfer characteristics of transistors based on p(g2T-TT) (V_{DS} = −0.1 V) and $Cu_3(HHTP)_2$ (V_{DS} = 0.1 V). (**E**) Voltage transfer characteristics (V_{in} versus V_{out}) of the complementary inverter at different V_{DD}. (**F**) Corresponding static gain ($\partial V_{out}/\partial V_{in}$) extracted from the voltage transfer curves. (**G**) Transient response of the inverter at V_{DD} = 0.4 V.

wearable electronics, point-of-care health care, and Internet of Things, flexible low-power circuits are increasingly desired. MOFECTs with high transconductance and low working voltage are promising for low-voltage inverters. Hence, as a proof-of-concept study, MOFECTs are implemented in flexible inverters. First, ambipolar inverters were built by integrating two MOFECTs on an ultrathin polyimide (PI) substrate to serve as the pull-up and pull-down transistors, respectively (fig. S19A). To enable flexible circuits, a thin layer of ion gel prepared by mixing poly(vinyl alcohol) with $CaCl_2$ solution was coated between the gate and the channel of each device to act as the electrolyte. The voltage transfer characteristics (V_{in} versus V_{out}) of the ambipolar inverter is presented in fig. S19B, which indicates that the device reaches a static gain G ($G = \partial V_{out}/\partial V_{in}$) of 4 at a low working voltage V_{DD} = 0.3 V (fig. S19C). The first-ever realization of an all-MOF inverter demonstrates the possibility of 2D c-MOFs for integrated circuits and is a key step for the implementations of 2D c-MOFs in microelectronics, while the device performance is expected to be further improved by device optimization and material design.

Next, a MOFECT in n-type mode was integrated with a p-type OECT for flexible complementary inverters (the fabrication process is presented in fig. S20). An enhancement-mode p-type OECT (pull-up) based on poly(2-(3,3′-bis(2-(2-(2-methoxyethoxy)ethoxy)ethoxy)-[2,2′-bithiophen]-5-yl)thieno [3,2-b]thiophene) [p(g2T-TT)] was chosen to connect with the n-type MOFECT (pull-down), as illustrated in Fig. 4A. p(g2T-TT) is a top performer with a high figure of merit (μC^*) in enhancement-mode p-type OECTs (*53*). Figure 4B presents the photograph of fabricated flexible inverter arrays laid on soft bracts of *Bougainvillea glabra*, and the optical photomicrograph of the patterned device channel is shown in Fig. 4C. The transfer characteristics of the p(g2T-TT)–based OECT and the n-type MOFECT are presented in Fig. 4D, which are well matched. The voltage transfer characteristics of the complementary inverter are shown in Fig. 4E. Notably, when V_{DD} is increased from 0.2 to 0.4 V, the peak static gain G ($G = \partial V_{out}/\partial V_{in}$) increases from 5 to 15 V V^{-1}, as presented in Fig. 4F, demonstrating the great potential of MOFECTs for low-voltage high-gain inverters.

Switching speed is a critical figure of merit for inverters and their applications. However, the transient response of electrochemical inverters is currently limited by the slow response of n-type OECTs (*54*, *55*). Our complementary inverters have a fast response speed of 0.79 ms (Fig. 4G) due to the fast response of both p-type OECT (0.34 ms; fig. S21A) and n-type MOFECT (0.26 ms; fig. S21B), which is much faster than the state-of-the-art complementary electrochemical inverters (fig. S22) (*10*, *54*–*57*). Notably, this bandwidth (1.27 kHz) is adequate for recording most physiological signals (<100 Hz) (*58*), which endows MOFECT-based inverters with great potential for wearable electronic applications.

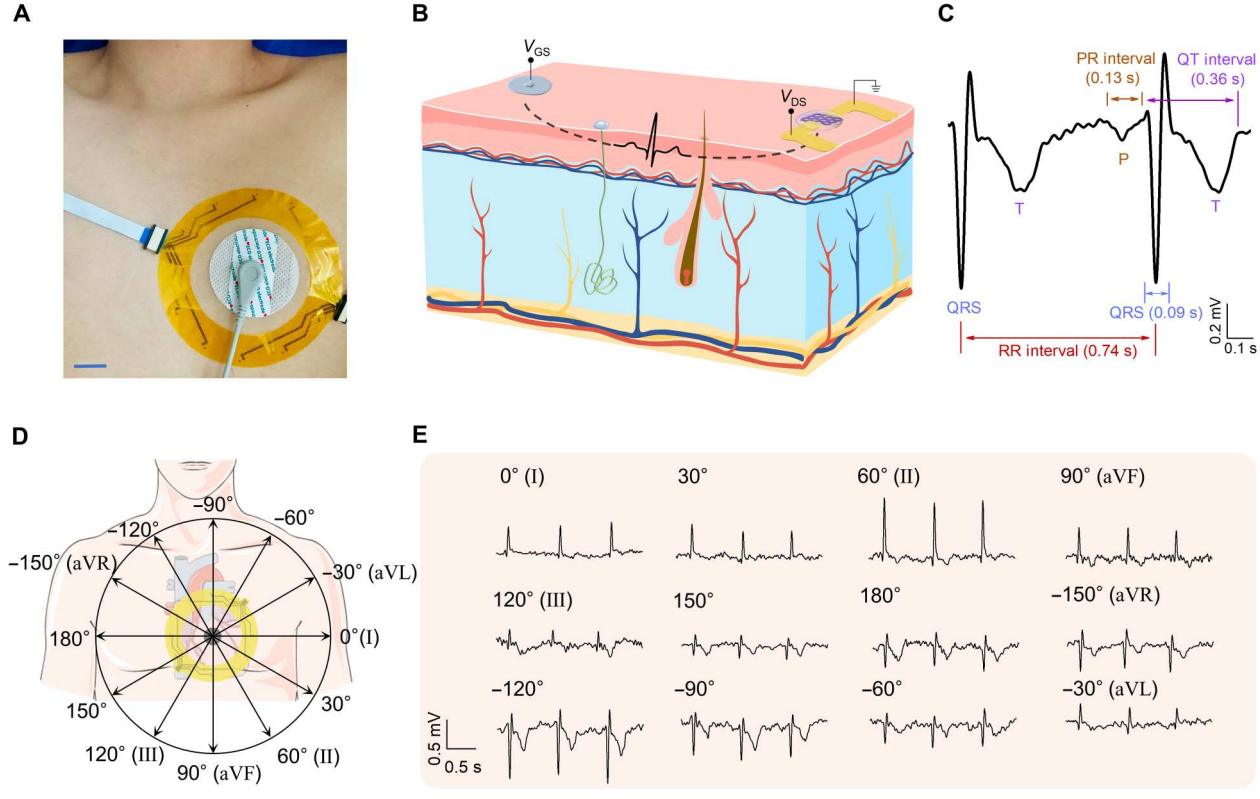

Fig. 5. Implementation of large-area MOFECT arrays in wearable ECG mapping. (**A**) Photograph of the ultraflexible MOFECT array attached on the chest of human. Scale bar, 2.0 cm. (**B**) Schematic diagram of the ECG measurement performed by placing a MOFECT and a shared gate on human skin. (**C**) A representative ECG waveform recorded by a MOFECT. (**D**) Distribution of the MOFECTs surrounding the heart. The graphic of human heart was adapted from Servier Medical Art templates, which are licensed under a Creative Commons Attribution 3.0 Unported License; https://smart.servier.com. (**E**) ECG signals recorded by 12 MOFECTs.

Implementation of MOFECTs in wearable electrophysiological mapping

The mapping of electrophysiological signals can provide critical information for cardiac disease diagnosis (*59*). Although in vivo electrophysiological mapping has been achieved by directly placing the devices on the surface of heart to record high-quality signals with spatial resolution (*60*, *61*), on-skin mapping of electrophysiological signals is rarely reported, which needs large-area sensor arrays with high sensitivity and uniform performance. MOFECT arrays were fabricated on ring-shaped ultrathin PI substrates (fig. S23) for monitoring ECG signals, in which 12 devices were evenly distributed on a circle with a radius of 5.0 cm. We found that the devices show high transconductance and uniformity, which is essential to ECG mapping with high reliability. To record ECG signals, the MOFECT array was directly adhered on the skin (Fig. 5A) by using a commercially available ECG gel, and a shared gate electrode (a commercial ECG electrode) was placed on the skin above the center of the heart. As diagrammatized in Fig. 5B, a very low gate voltage (0.06 V) was applied to the MOFECT to make it operate with a maximum transconductance, and the electrical potential differences (ECG signals) between the shared gate and the MOFECTs surrounding the heart can be monitored by recording the channel currents. Figure 5C is a representative ECG signal recorded by a MOFECT device, clearly showing the typical components including the P wave, the QRS complex, and the T wave. The key features of the ECG waveform including QRS duration (0.09 s), PR interval (0.13 s), QT interval (0.36 s), and RR interval (0.74 s) are all in normal ranges, indicating a normal sinus rhythm (81 beats/min) of an adult (*62*).

The 12 MOFECTs on the substrate offer a straightforward way to monitor the ECG signals of the heart from different angles (Fig. 5D), which can provide meaningful information for the diagnosis of cardiac diseases like cardiac arrhythmias and myocardial ischemia (*62*). The recorded signals (Fig. 5E, the raw channel current signals are shown in fig. S24) show distinct waveforms that could be related to different regions of the heart conventionally monitored by a standard 12-lead ECG facility. The six limb leads (I, II, aVF, III, aVR, and aVL) in standard 12-lead ECG measurements correspond to the six different directions, including 0°, 60°, 90°, 120°, −150°, and −30°, which have been covered by six of our devices shown in Fig. 5D. As the depolarization wave normally spreads through the ventricles from −120° to 60° (II) (*63*), the signals along the four directions [0°(I), 60°(II), 90°(aVF), and 120°(III)] of the subject demonstrate significant upward QRS complexes, while the signal along −150°(aVR) shows a downward one due to its opposite direction, which are similar to the waveforms obtained from a conventional ECG testing facility. Because our device is portable and lightweight, it could be used for continuous ECG monitoring needed by patients with heart diseases, emergency rescue, or wearable fitness trackers, which cannot be achieved with conventional multilead ECG facilities.

DISCUSSION

We find that 2D c-MOF $Cu_3(HHTP)_2$ is an ideal channel material of ECTs because of its porous crystal structure and high carrier mobility. On the basis of a convenient liquid-phase deposition of highly oriented $Cu_3(HHTP)_2$, large-scale MOFECT arrays have been realized with a high yield and a uniform mobility distribution. The MOFECTs exhibit balanced ambipolar behavior, in which the bulk conductivity of $Cu_3(HHTP)_2$ channel can be notably modulated through cations or anions doping from the electrolyte. The highly oriented $Cu_3(HHTP)_2$ films provide vertical ion channels across the whole films, leading to a high volumetric capacitance, convenient ion transfer, and a fast response speed of the devices. Different from ECTs based on polymers, where the swelling of polymers in aqueous electrolytes needs to be judiciously controlled to balance efficient bulk ion doping and stable operation, MOFECTs show negligible swelling due to the high crystallinity of the $Cu_3(HHTP)_2$ films, offering the devices with good operational stability. MOFECTs have been successfully deployed in ultrathin flexible circuits including all-MOF ambipolar inverters and complementary inverters, which exhibit a high voltage gain up to 15 V V^{-1} and fast switching (1.27 kHz) under a low working voltage of 0.4 V. Benefitting from the high transconductance and convenient large-area fabrication, ultraflexible MOFECT arrays have been fabricated and used for on-skin mapping of ECG signals along different directions. This work demonstrates the great potential of MOFECTs for large-area and flexible electronics.

MATERIALS AND METHODS

Materials

HHTP was purchased from J&K Scientific Ltd.; copper acetate and calcium chloride ($CaCl_2$) were purchased from Sigma-Aldrich Co.; AZ 5214E and SU-8 2002 photoresist were purchased from Micro-Chemicals GmbH; poly(vinyl alcohol) 1788 was purchased from Shanghai Macklin Biochemical Co. Ltd.; and p(g2T-TT) was synthesized as previously reported (*53*). The commercial ECG electrodes (Ag/AgCl) were purchased from Hangzhou XUNDA Co. Ltd., and the ECG gel on MOFECT is the same as on the electrodes.

Characterizations of $Cu_3(HHTP)_2$

The film thickness of $Cu_3(HHTP)_2$ was measured using a Bruker DektakXT Surface Profiler. A field emission scanning electron microscope (Tescan MAIA3) was used to characterize the morphology of $Cu_3(HHTP)_2$ films, and the topography of $Cu_3(HHTP)_2$ film was observed using a Scanning Probe Microscope (Bruker NanoScope 8). GIXRD patterns of $Cu_3(HHTP)_2$ were obtained using an x-ray diffraction system (Rigaku SmartLab) with an incidence angle of 0.4°. The average gain size of the $Cu_3(HHTP)_2$ was estimated on the basis of W-H method (*33*). A W-H plot ($\beta_{hkl}\cos\theta = \frac{k\lambda}{D} + 4\varepsilon\sin\theta$) is drawn by plotting $\beta_{hkl}\cos\theta$ on y axis against 4sin on x axis (fig. S1B), where β_{hkl} is the full width at half maximum of each XRD peak, k is the shape factor, λ is the wavelength of x-ray source, D is the crystallite size, and ε is the strain. The grain size can be calculated from the y-intercept of the linear fit. Transmission electron microscope (TEM) images of $Cu_3(HHTP)_2$ film were performed on a JEOL JEM-2100F TEM/STEM. The contact angle was measured using an Ossila Contact Angle Goniometer. The ex situ XPS of $Cu_3(HHTP)_2$ at different states were obtained by Thermo Fisher Scientific Nexsa G2 XPS System. The MOF film was prepared on an indium tin oxide substrate. The ion doping of the film was carried out by immersing the sample in 0.05 M $CaCl_2$ and applying a bias (0.05 V for n-type doping and −0.5 V for p-type doping) on a reference Ag/AgCl electrode for 60 s. The structural properties including pore diameter, surface area, pore volume, mass density, porosity, and volume-to-surface rate of the

$Cu_3(HHTP)_2$ were calculated using Zeo++ software (*64*) with a nitrogen probe radius of 1.86 Å. The lattice parameters and atomic coordinates of the $Cu_3(HHTP)_2$ were obtained from the literature (*32*). The calculated structural parameters are summarized in table S2.

Microfabrication of MOFECTs

The microfabrication process flow of the $Cu_3(HHTP)_2$-based MOFECT is shown in Fig. 1E. AZ 5214E photoresist was spin-coated on the surface of a well-cleaned glass substrate, exposed to ultraviolet light using SUSS MA6 Mask Aligner, and then developed by AZ 300 MIF developer. Ten nanometers of chromium (Cr) and 100 nm of gold (Au) were subsequently deposited on the substrate using magnetron sputtering, followed by a lift-off process in acetone. A layer of Al_2O_3 (10 nm) was deposited using atomic layer deposition and patterned via similar photolithography and lift-off processes, serving as the insulation layer. A sacrificial SU-8 layer (SU-2002) was then spin-coated and patterned on the substrate for the patterning of 2D MOFs. The in situ growth of $Cu_3(HHTP)_2$ films was conducted on the basis of a layer-by-layer assembling process (*32*). Specifically, after O_2 plasma treatment, the substrate was alternatively steeped in 1 mM $Cu(OAc)_2$ ethanolic solution and 0.1 mM HHTP ethanolic solution for 20 and 40 min, respectively. Each immersing step was followed by a carefully washing process using pure ethanol. After obtaining desired film thickness, the SU-8 layer was peeled off. Last, the devices were annealed at 85°C for 30 min in a glove box filled with high-purity N_2.

Fabrication of inverters

The fabrication of all-MOF inverters on ultrathin PI substrates is the same as that of MOFECTs. The fabrication process of the complementary inverter containing a MOFECT and an OECT is presented in fig. S20. Specifically, a layer of AZ 5214E was deposited on the PI substrate with patterned metal electrodes, Al_2O_3 layer, and SU-8 layer. p(g2T-TT) was spin-coated on the patterned AZ 5214E and annealed at 100°C for 30 min in a glove box filled with high-purity N_2. After removing the unwanted p(g2T-TT) on the photoresist by acetone washing, the substrate was encapsulated for the growth of 2D MOF. After fabricating a MOFECT using the aforementioned process, a complementary inverter was obtained. The device geometry (channel length L, channel width W, and channel thickness d) of the transistors is optimized to obtain well-matched transfer characteristics.

Electrical characterizations

The output ($I_{DS} - V_{DS}$) and transfer characteristics ($I_{DS} - V_G$) were measured by two Keithley source meters (Keithley 2400). For the transient response of MOFECTs, an Agilent 33220A waveform generator was used to supply the gate voltage (V_G) pulse, and a SR570 low-noise current preamplifier was used to provide a drain bias (V_{DS}) and convert the channel current into voltage signals. The channel current response was recorded by a Tektronix TBS2072 digital storage oscilloscope. The operational stability of MOFECTs was performed by monitoring the channel current under continuous gate voltage pulses.

The voltage transfer curves of inverters were measured using a Keithley 4200A-SCS Parameter Analyzer. For the transient response of inverters, an Agilent 33220A waveform generator was used to supply an input voltage (V_{in}) pulse, a Keithley 2400 source meter was used to supply a V_{DD}, and the output voltage (V_{out}) was recorded using a Tektronix TBS2072 digital storage oscilloscope. All the electrical measurements were performed in ambient air at room temperature.

Electrochemical measurements

EIS measurements of the $Cu_3(HHTP)_2$ films were performed with a three-electrode system using a Zahner Zennium pro electrochemical workstation. 2D MOF films were prepared on the Au electrodes, serving as the working electrode. A platinum wire was used as the counter electrode, and Ag/AgCl was used as the reference electrode. $CaCl_2$ aqueous solution (0.05 M) was used as the electrolyte. The amplitude of the AC voltage is 10.0 mV, and the frequency range is from 0.5 Hz to 1.0 MHz. The capacitance of the $Cu_3(HHTP)_2$ film was obtained by fitting the EIS to an equivalent circuit composed of a serial resistance R_s, a parallel resistance R_p, and a parallel constant phase element (CPE) $R_s(R_p\|CPE)$. A CPE, commonly used in porous materials, is used to extract the capacitance of the $Cu_3(HHTP)_2$ film (*65*). All the electrochemical measurements were performed in ambient air at room temperature.

ECG mapping

For wearable ECG mapping, the MOFECT array fabricated on a PI substrate was directly adhered on the skin by using commercially available ECG gels, and a shared gate (a commercially available ECG electrode) was placed on the center of the heart. The electrical potential differences (ECG signals) between the shared gate above the center of the heart and the MOFECTs surrounding the heart can be monitored by recording the channel currents, which can be transferred into voltage signals according to the transconductance of MOFECTs. A Keithley 2400 source meter was used to supply a gate voltage (V_{GS}) to make MOFECTs operate with maximum transconductance, and a SR570 low-noise current preamplifier was used to provide a drain bias (V_{DS}) and convert the channel current into voltage signals. The channel current response was recorded by a Tektronix TBS2072 digital storage oscilloscope. The measured signals were filtered by a bandpass filter between 0.5 and 40 Hz. The measurements were taken in accordance with the Institutional Review Board guidelines, and informed written consent was obtained from the participant.

Supplementary Materials

This PDF file includes:

Figs. S1 to S24
Tables S1 and S2

REFERENCES AND NOTES

1. Z. Yan, D. Xu, Z. Lin, P. Wang, B. Cao, H. Ren, F. Song, C. Wan, L. Wang, J. Zhou, X. Zhao, J. Chen, Y. Huang, X. Duan, Highly stretchable van der Waals thin films for adaptable and breathable electronic membranes. *Science* **375**, 852–859 (2022).
2. S. Park, S. W. Heo, W. Lee, D. Inoue, Z. Jiang, K. Yu, H. Jinno, D. Hashizume, M. Sekino, T. Yokota, K. Fukuda, K. Tajima, T. Someya, Self-powered ultra-flexible electronics via nano-grating-patterned organic photovoltaics. *Nature* **561**, 516–521 (2018).
3. A. B. Calia, E. Masvidal-Codina, T. M. Smith, N. Schafer, D. Rathore, E. Rodriguez-Lucas, X. Illa, J. M. De la Cruz, E. Del Corro, E. Prats-Alfonso, D. Viana, J. Bousquet, C. Hebert, J. Martinez-Aguilar, J. R. Sperling, M. Drummond, A. Halder, A. Dodd, K. Barr, S. Savage, J. Fornell, J. Sort, C. Guger, R. Villa, K. Kostarelos, R. C. Wykes, A. Guimera-Brunet, J. A. Garrido, Full-band-width electrophysiology of seizures and epileptiform activity enabled by flexible graphene microtransistor depth neural probes. *Nat. Nanotechnol.* **17**, 301–309 (2022).

4. E. Masvidal-Codina, X. Illa, M. Dasilva, A. B. Calia, T. Dragojevic, E. E. Vidal-Rosas, E. Prats-Alfonso, J. Martinez-Aguilar, J. M. De la Cruz, R. Garcia-Cortadella, P. Godignon, G. Rius, A. Camassa, E. Del Corro, J. Bousquet, C. Hebert, T. Durduran, R. Villa, M. V. Sanchez-Vives, J. A. Garrido, A. Guimera-Brunet, High-resolution mapping of infraslow cortical brain activity enabled by graphene microtransistors. *Nat. Mater.* **18**, 280–288 (2019).
5. J. Chen, W. Huang, D. Zheng, Z. Xie, X. Zhuang, D. Zhao, Y. Chen, N. Su, H. Chen, R. M. Pankow, Z. Gao, J. Yu, X. Guo, Y. Cheng, J. Strzalka, X. Yu, T. J. Marks, A. Facchetti, Highly stretchable organic electrochemical transistors with strain-resistant performance. *Nat. Mater.* **21**, 564–571 (2022).
6. E. J. Fuller, S. T. Keene, A. Melianas, Z. Wang, S. Agarwal, Y. Li, Y. Tuchman, C. D. James, M. J. Marinella, J. J. Yang, A. Salleo, A. A. Talin, Parallel programming of an ionic floating-gate memory array for scalable neuromorphic computing. *Science* **364**, 570–574 (2019).
7. Y. van de Burgt, E. Lubberman, E. J. Fuller, S. T. Keene, G. C. Faria, S. Agarwal, M. J. Marinella, A. A. Talin, A. Salleo, A non-volatile organic electrochemical device as a low-voltage artificial synapse for neuromorphic computing. *Nat. Mater.* **16**, 414–418 (2017).
8. J. Lenz, F. Del Giudice, F. R. Geisenhof, F. Winterer, R. T. Weitz, Vertical, electrolyte-gated organic transistors show continuous operation in the MA cm^{-2} regime and artificial synaptic behaviour. *Nat. Nanotechnol.* **14**, 579–585 (2019).
9. Y. Kim, A. Chortos, W. Xu, Y. Liu, J. Y. Oh, D. Son, J. Kang, A. M. Foudeh, C. Zhu, Y. Lee, S. Niu, J. Liu, R. Pfattner, Z. Bao, T. W. Lee, A bioinspired flexible organic artificial afferent nerve. *Science* **360**, 998–1003 (2018).
10. Y. Yao, W. Huang, J. H. Chen, G. Wang, H. M. Chen, X. M. Zhuang, Y. B. Ying, J. F. Ping, T. J. Marks, A. Facchetti, Flexible complementary circuits operating at sub-0.5 V via hybrid organic inorganic electrolyte-gated transistors. *Proc. Natl. Acad. Sci. U.S.A.* **118**, e2111790118 (2021).
11. P. Andersson Ersman, R. Lassnig, J. Strandberg, D. Tu, V. Keshmiri, R. Forchheimer, S. Fabiano, G. Gustafsson, M. Berggren, All-printed large-scale integrated circuits based on organic electrochemical transistors. *Nat. Commun.* **10**, 5053 (2019).
12. S. H. Kim, K. Hong, W. Xie, K. H. Lee, S. Zhang, T. P. Lodge, C. D. Frisbie, Electrolyte-gated transistors for organic and printed electronics. *Adv. Mater.* **25**, 1822–1846 (2013).
13. F. Torricelli, D. Z. Adrahtas, Z. Bao, M. Berggren, F. Biscarini, A. Bonfiglio, C. A. Bortolotti, C. D. Frisbie, E. Macchia, G. G. Malliaras, I. McCulloch, M. Moser, T. Q. Nguyen, R. M. Owens, A. Salleo, A. Spanu, L. Torsi, Electrolyte-gated transistors for enhanced performance bioelectronics. *Nat. Rev. Methods Primers* **1**, 1–24 (2021).
14. H. Liu, A. N. Yang, J. J. Song, N. X. Wang, P. Y. Lam, Y. L. Li, H. K. W. Law, F. Yan, Ultrafast, sensitive, and portable detection of COVID-19 IgG using flexible organic electrochemical transistors. *Sci. Adv.* **7**, eabg8387 (2021).
15. K. Guo, S. Wustoni, A. Koklu, E. Diaz-Galicia, M. Moser, A. Hama, A. A. Alqahtani, A. N. Ahmad, F. S. Alhamlan, M. Shuaib, A. Pain, I. McCulloch, S. T. Arold, R. Grunberg, S. Inal, Rapid single-molecule detection of COVID-19 and MERS antigens via nanobody-functionalized organic electrochemical transistors. *Nat. Biomed. Eng.* **5**, 666–677 (2021).
16. P. Lin, F. Yan, Organic thin-film transistors for chemical and biological sensing. *Adv. Mater.* **24**, 34–51 (2012).
17. S. Inal, G. G. Malliaras, J. Rivnay, Benchmarking organic mixed conductors for transistors. *Nat. Commun.* **8**, 1767 (2017).
18. F. Yan, M. Zhang, J. Li, Solution-gated graphene transistors for chemical and biological sensors. *Adv. Healthc. Mater.* **3**, 313–331 (2014).
19. A. G. Kelly, T. Hallam, C. Backes, A. Harvey, A. S. Esmaeily, I. Godwin, J. Coelho, V. Nicolosi, J. Lauth, A. Kulkarni, S. Kinge, L. D. Siebbeles, G. S. Duesberg, J. N. Coleman, All-printed thin-film transistors from networks of liquid-exfoliated nanosheets. *Science* **356**, 69–73 (2017).
20. F. Zare Bidoky, B. Tang, R. Ma, K. S. Jochem, W. J. Hyun, D. Song, S. J. Koester, T. P. Lodge, C. D. Frisbie, Sub-3 V ZnO electrolyte-gated transistors and circuits with screen-printed and photo-crosslinked ion gel gate dielectrics: New routes to improved performance. *Adv. Funct. Mater.* **30**, 1902028 (2020).
21. J. Rivnay, S. Inal, A. Salleo, R. M. Owens, M. Berggren, G. G. Malliaras, Organic electrochemical transistors. *Nat. Rev. Mater.* **3**, 1–14 (2018).
22. B. D. Paulsen, K. Tybrandt, E. Stavrinidou, J. Rivnay, Organic mixed ionic-electronic conductors. *Nat. Mater.* **19**, 13–26 (2020).
23. D. Khodagholy, J. Rivnay, M. Sessolo, M. Gurfinkel, P. Leleux, L. H. Jimison, E. Stavrinidou, T. Herve, S. Sanaur, R. M. Owens, G. G. Malliaras, High transconductance organic electrochemical transistors. *Nat. Commun.* **4**, 2133 (2013).
24. J. H. Dou, M. Q. Arguilla, Y. Luo, J. Li, W. Zhang, L. Sun, J. L. Mancuso, L. Yang, T. Chen, L. R. Parent, G. Skorupskii, N. J. Libretto, C. Sun, M. C. Yang, P. V. Dip, E. J. Brignole, J. T. Miller, J. Kong, C. H. Hendon, J. Sun, M. Dinca, Atomically precise single-crystal structures of electrically conducting 2D metal-organic frameworks. *Nat. Mater.* **20**, 222–228 (2021).
25. M. Wang, R. Dong, X. Feng, Two-dimensional conjugated metal-organic frameworks (2D c-MOFs): Chemistry and function for MOFtronics. *Chem. Soc. Rev.* **50**, 2764–2793 (2021).
26. S. Bi, H. Banda, M. Chen, L. Niu, M. Chen, T. Wu, J. Wang, R. Wang, J. Feng, T. Chen, M. Dinca, A. A. Kornyshev, G. Feng, Molecular understanding of charge storage and charging dynamics in supercapacitors with MOF electrodes and ionic liquid electrolytes. *Nat. Mater.* **19**, 552–558 (2020).
27. M. E. Ziebel, C. A. Gaggioli, A. B. Turkiewicz, W. Ryu, L. Gagliardi, J. R. Long, Effects of covalency on anionic redox chemistry in semiquinoid-based metal-organic frameworks. *J. Am. Chem. Soc.* **142**, 2653–2664 (2020).
28. K. W. Nam, S. S. Park, R. Dos Reis, V. P. Dravid, H. Kim, C. A. Mirkin, J. F. Stoddart, Conductive 2D metal-organic framework for high-performance cathodes in aqueous rechargeable zinc batteries. *Nat. Commun.* **10**, 1–10 (2019).
29. X. Huang, P. Sheng, Z. Tu, F. Zhang, J. Wang, H. Geng, Y. Zou, C. A. Di, Y. Yi, Y. Sun, W. Xu, D. Zhu, A two-dimensional π–d conjugated coordination polymer with extremely high electrical conductivity and ambipolar transport behaviour. *Nat. Commun.* **6**, 7408 (2015).
30. G. Wu, J. Huang, Y. Zang, J. He, G. Xu, Porous field-effect transistors based on a semiconductive metal-organic framework. *J. Am. Chem. Soc.* **139**, 1360–1363 (2017).
31. D. Sheberla, J. C. Bachman, J. S. Elias, C. J. Sun, Y. Shao-Horn, M. Dinca, Conductive MOF electrodes for stable supercapacitors with high areal capacitance. *Nat. Mater.* **16**, 220–224 (2017).
32. X. Song, X. Wang, Y. Li, C. Zheng, B. Zhang, C. A. Di, F. Li, C. Jin, W. Mi, L. Chen, W. Hu, 2D semiconducting metal-organic framework thin films for organic spin valves. *Angew. Chem. Int. Ed.* **59**, 1118–1123 (2020).
33. V. Mote, Y. Purushotham, B. Dole, Williamson-Hall analysis in estimation of lattice strain in nanometer-sized ZnO particles. *J. Theor. Appl. Phys.* **6**, 1–8 (2012).
34. J. Rivnay, P. Leleux, M. Ferro, M. Sessolo, A. Williamson, D. A. Koutsouras, D. Khodagholy, M. Ramuz, X. Strakosas, R. M. Owens, C. Benar, J. M. Badier, C. Bernard, G. G. Malliaras, High-performance transistors for bioelectronics through tuning of channel thickness. *Sci. Adv.* **1**, e1400251 (2015).
35. H. Y. Wu, C. Y. Yang, Q. Li, N. B. Kolhe, X. Strakosas, M. A. Stoeckel, Z. Wu, W. Jin, M. Savvakis, R. Kroon, D. Tu, H. Y. Woo, M. Berggren, S. A. Jenekhe, S. Fabiano, Influence of molecular weight on the organic electrochemical transistor performance of ladder-type conjugated polymers. *Adv. Mater.* **34**, e2106235 (2022).
36. K. Feng, W. Shan, J. Wang, J. W. Lee, W. Yang, W. Wu, Y. Wang, B. J. Kim, X. Guo, H. Guo, Cyano-functionalized n-type polymer with high electron mobility for high-performance organic electrochemical transistors. *Adv. Mater.* **34**, e2201340 (2022).
37. D. A. Bernards, G. G. Malliaras, Steady-state and transient behavior of organic electrochemical transistors. *Adv. Funct. Mater.* **17**, 3538–3544 (2007).
38. J. T. Friedlein, R. R. McLeod, J. Rivnay, Device physics of organic electrochemical transistors. *Org. Electron.* **63**, 398–414 (2018).
39. J. Li, M. Chen, A. Samad, H. Dong, A. Ray, J. Zhang, X. Jiang, U. Schwingenschlogl, J. Domke, C. Chen, Y. Han, T. Fritz, R. S. Ruoff, B. Tian, X. Zhang, Wafer-scale single-crystal monolayer graphene grown on sapphire substrate. *Nat. Mater.* **21**, 740–747 (2022).
40. N. Li, Q. Q. Wang, C. Shen, Z. Wei, H. Yu, J. Zhao, X. B. Lu, G. L. Wang, C. L. He, L. Xie, J. Q. Zhu, L. J. Du, R. Yang, D. X. Shi, G. Y. Zhang, Large-scale flexible and transparent electronics based on monolayer molybdenum disulfide field-effect transistors. *Nat. Electron.* **3**, 711–717 (2020).
41. J. S. Tang, Q. Cao, G. Tulevski, K. A. Jenkins, L. Nela, D. B. Farmer, S. J. Han, Flexible CMOS integrated circuits based on carbon nanotubes with sub-10 ns stage delays. *Nat. Electron.* **1**, 191–196 (2018).
42. Y. Cui, Z. H. Zhong, D. L. Wang, W. U. Wang, C. M. Lieber, High performance silicon nanowire field effect transistors. *Nano Lett.* **3**, 149–152 (2003).
43. A. Giovannitti, C. B. Nielsen, D.-T. Sbircea, S. Inal, M. Donahue, M. R. Niazi, D. A. Hanifi, A. Amassian, G. G. Malliaras, J. Rivnay, N-type organic electrochemical transistors with stability in water. *Nat. Commun.* **7**, 1–10 (2016).
44. D. Ohayon, A. Savva, W. Du, B. D. Paulsen, I. Uguz, R. S. Ashraf, J. Rivnay, I. McCulloch, S. Inal, Influence of side chains on the n-type organic electrochemical transistor performance. *ACS Appl. Mater. Interfaces* **13**, 4253–4266 (2021).
45. J. Surgailis, A. Savva, V. Druet, B. D. Paulsen, R. H. Wu, A. Hamidi-Sakr, D. Ohayon, G. Nikiforidis, X. X. Chen, I. McCulloch, J. Rivnay, S. Inal, Mixed conduction in an n-type organic semiconductor in the absence of hydrophilic side-chains. *Adv. Funct. Mater.* **31**, 2010165 (2021).
46. S. Kondrat, P. Wu, R. Qiao, A. A. Kornyshev, Accelerating charging dynamics in subnanometre pores. *Nat. Mater.* **13**, 387–393 (2014).
47. P. M. Biesheuvel, M. Z. Bazant, Nonlinear dynamics of capacitive charging and desalination by porous electrodes. *Phys. Rev. E Stat. Nonlin. Soft Matter Phys.* **81**, 031502 (2010).
48. S. Griggs, A. Marks, H. Bristow, I. McCulloch, n-Type organic semiconducting polymers: Stability limitations, design considerations and applications. *J. Mater. Chem. C* **9**, 8099–8128 (2021).
49. R. Giridharagopal, L. Q. Flagg, J. S. Harrison, M. E. Ziffer, J. Onorato, C. K. Luscombe, D. S. Ginger, Electrochemical strain microscopy probes morphology-induced variations in

ion uptake and performance in organic electrochemical transistors. *Nat. Mater.* **16**, 737–742 (2017).
50. A. A. Szumska, I. P. Maria, L. Q. Flagg, A. Savva, J. Surgailis, B. D. Paulsen, D. Moia, X. Chen, S. Griggs, J. T. Mefford, R. B. Rashid, A. Marks, S. Inal, D. S. Ginger, A. Giovannitti, J. Nelson, Reversible electrochemical charging of n-type conjugated polymer electrodes in aqueous electrolytes. *J. Am. Chem. Soc.* **143**, 14795–14805 (2021).
51. L. Q. Flagg, C. G. Bischak, J. W. Onorato, R. B. Rashid, C. K. Luscombe, D. S. Ginger, Polymer crystallinity controls water uptake in glycol side-chain polymer organic electrochemical transistors. *J. Am. Chem. Soc.* **141**, 4345–4354 (2019).
52. T. Leydecker, Z. M. Wang, F. Torricelli, E. Orgiu, Organic-based inverters: Basic concepts, materials, novel architectures and applications. *Chem. Soc. Rev.* **49**, 7627–7670 (2020).
53. A. Giovannitti, D. T. Sbircea, S. Inal, C. B. Nielsen, E. Bandiello, D. A. Hanifi, M. Sessolo, G. G. Malliaras, I. McCulloch, J. Rivnay, Controlling the mode of operation of organic transistors through side-chain engineering. *Proc. Natl. Acad. Sci. U.S.A.* **113**, 12017–12022 (2016).
54. R. B. Rashid, W. Du, S. Griggs, I. P. Maria, I. McCulloch, J. Rivnay, Ambipolar inverters based on cofacial vertical organic electrochemical transistor pairs for biosignal amplification. *Sci. Adv.* **7**, eabh1055 (2021).
55. H. Sun, M. Vagin, S. Wang, X. Crispin, R. Forchheimer, M. Berggren, S. Fabiano, Complementary logic circuits based on high-performance n-type organic electrochemical transistors. *Adv. Mater.* **30**, 1704916 (2018).
56. P. Romele, P. Gkoupidenis, D. A. Koutsouras, K. Lieberth, Z. M. Kovacs-Vajna, P. W. M. Blom, F. Torricelli, Multiscale real time and high sensitivity ion detection with complementary organic electrochemical transistors amplifier. *Nat. Commun.* **11**, 3743 (2020).
57. L. Travaglini, A. P. Micolich, C. Cazorla, E. Zeglio, A. Lauto, D. Mawad, Single-material OECT-based flexible complementary circuits featuring polyaniline in both conducting channels. *Adv. Funct. Mater.* **31**, 2007205 (2021).
58. P. Leleux, J. Rivnay, T. Lonjaret, J. M. Badier, C. Benar, T. Herve, P. Chauvel, G. G. Malliaras, Organic electrochemical transistors for clinical applications. *Adv. Healthc. Mater.* **4**, 142–147 (2015).
59. R. Dubois, A. J. Shah, M. Hocini, A. Denis, N. Derval, H. Cochet, F. Sacher, L. Bear, J. Duchateau, P. Jais, M. Haissaguerre, Non-invasive cardiac mapping in clinical practice: Application to the ablation of cardiac arrhythmias. *J. Electrocardiol.* **48**, 966–974 (2015).
60. K. Sim, F. Ershad, Y. C. Zhang, P. Y. Yang, H. Shim, Z. Y. Rao, Y. T. Lu, A. Thukral, A. Elgalad, Y. T. Xi, B. Z. Tian, D. A. Taylor, C. J. Yu, An epicardial bioelectronic patch made from soft rubbery materials and capable of spatiotemporal mapping of electrophysiological activity. *Nat. Electron.* **3**, 775–784 (2020).
61. W. Lee, S. Kobayashi, M. Nagase, Y. Jimbo, I. Saito, Y. Inoue, T. Yambe, M. Sekino, G. G. Malliaras, T. Yokota, M. Tanaka, T. Someya, Nonthrombogenic, stretchable, active multielectrode array for electroanatomical mapping. *Sci. Adv.* **4**, eaau2426 (2018).
62. M. G. Khan, *Rapid ECG Interpretation*. (Springer, 2008).
63. J. Hampton, J. Hampton, *The ECG Made Easy E-book*. (Elsevier Health Sciences, 2019).
64. T. F. Willems, C. Rycroft, M. Kazi, J. C. Meza, M. Haranczyk, Algorithms and tools for high-throughput geometry-based analysis of crystalline porous materials. *Microporous Mesoporous Mater.* **149**, 134–141 (2012).
65. R. B. Rashid, A. M. Evans, L. A. Hall, R. R. Dasari, E. K. Roesner, S. R. Marder, D. M. D'Allesandro, W. R. Dichtel, J. Rivnay, A semiconducting two-dimensional polymer as an organic electrochemical transistor active layer. *Adv. Mater.* **34**, 2110703 (2022).

Acknowledgments
Funding: This work is financially supported by Research Grants Council (RGC) of Hong Kong, China (project no. 15210319), Innovation and Technology Commission of Hong Kong (project no. MRP/040/18X), and The Hong Kong Polytechnic University (project no. ZE2X and YW4Z).
Author contributions: F.Y. conceived the experiments. J.S. carried most experiments and data analysis. H.L., Z.Z., and C.-k.L. assisted in device fabrication and characterization. X.G. and Y.Z. did TEM characterization. S.G., A.M., and I.M. synthesized p(g2T-TT) polymer. H.K.-w.L. has contributed to the analysis of ECG signals. The manuscript was written by J.S. and F.Y. All authors contributed to manuscript review, revision, and finalization. **Competing interests:** The authors declare that they have no competing interests. **Data and materials availability:** All data needed to evaluate the conclusions in the paper are present in the paper and/or the Supplementary Materials.

Submitted 15 July 2022
Accepted 12 December 2022
Published 11 January 2023
10.1126/sciadv.add9627

ScienceAdvances

2D metal-organic frameworks for ultraflexible electrochemical transistors with high transconductance and fast response speeds

Jiajun Song, Hong Liu, Zeyu Zhao, Xuyun Guo, Chun-ki Liu, Sophie Griggs, Adam Marks, Ye Zhu, Helen Ka-wai Law, Iain McCulloch, and Feng Yan

Sci. Adv., **9** (2), eadd9627.
DOI: 10.1126/sciadv.add9627

Science Advances (ISSN) is published by the American Association for the Advancement of Science. 1200 New York Avenue NW, Washington, DC 20005. The title *Science Advances* is a registered trademark of AAAS.